30th AIAA Applied Aerodynamics Conference
25-28 June 2012, New Orleans, Louisiana 2012-2768

# Glide and Powered Flight Characteristics of Micro Air Vehicles from Experimental Measurements

Arjun H. Rao*, Daniel V. Uhlig†, and Michael S. Selig‡
*University of Illinois at Urbana-Champaign, Urbana, IL 61801, USA*

**Aerodynamic characteristics of Micro Air Vehicles (MAVs) is not well addressed in aeronautics literature, and more experimental data are required to help better understand the behavior of fixed-wing MAVs. In the current research, aerodynamic characteristics of two MAVs were measured using a motion tracking system. The aircraft used were flat-foam surface, highly-aerobatic, micro RC models. Tests were conducted in glide and powered flight conditions to assess the aerodynamic performance of a commercially manufactured Extra 300 3D and a custom-built Extra 260 with wingspans of 42.67 cm (16.8 in) and 41.27 cm (16.25 in), respectively. The results presented show the longitudinal aerodynamic characteristics of the MAVs over a range of angle of attack at a nominal Reynolds number of 25,000. The influence of low Reynolds numbers effects on the aerodynamic characteristics and performance of the aircraft are discussed. The aerodynamic characteristics in powered flight were analyzed by testing the Extra 300 3D over a range of propeller advance ratios. Results indicate an increase in the slope of the lift curve and reduction in drag with decreasing propeller advance ratios.**

## Nomenclature

| | | |
|---|---|---|
| $a_x$, $a_y$, $a_z$ | = | body-axis translational acceleration |
| $\mathcal{AR}$ | = | aspect ratio |
| $b$ | = | wingspan |
| $c$ | = | wing mean aerodynamic chord |
| $C_D$ | = | drag coefficient ($D/\frac{1}{2}\rho V^2 S_{ref}$) |
| $C_{D_o}$ | = | parasite drag coefficient |
| $C_L$ | = | lift coefficient ($L/\frac{1}{2}\rho V^2 S_{ref}$) |
| $C_{L_\alpha}$ | = | lift curve slope |
| $C_T$ | = | thrust coefficient ($T/\rho n^2 {D_p}^4$) |
| $D$ | = | drag |
| $D_p$ | = | propeller diameter |
| $\mathbf{F}$ | = | force |
| $J$ | = | advance ratio |
| $L$ | = | lift |
| $m$ | = | airplane mass |
| $n$ | = | propeller rotational speed (rev/sec) |
| $p$, $q$, $r$ | = | roll, pitch and yaw rates |
| $\mathbf{R}$ | = | transformation or rotation matrix |
| $Re$ | = | Reynolds number based on mean aerodynamic chord ($Vc/\nu$) |
| $S_f$ | = | fuselage area |
| $S_{prop}$ | = | propeller area |
| $S_{ref}$ | = | reference area (wing area + fuselage area) |
| $S_h$ | = | tail area |

*Graduate Student, Department of Aerospace Engineering and AIAA Student Member
†Graduate Student, Department of Aerospace Engineering and AIAA Student Member
‡Associate Professor, Department of Aerospace Engineering, and AIAA Senior Member


Copyright © 2012 by the author. Published by the American Institute of Aeronautics and Astronautics, Inc., with permission.

| | | |
|---|---|---|
| $S_w$ | = | wing area |
| $u$, $v$, $w$ | = | body-fixed translational velocity |
| $V$ | = | inertial speed |
| $\alpha$ | = | angle of attack |
| $\dot{\alpha}$ | = | angle of attack rate |
| $\beta$ | = | sideslip angle |
| $\dot{\beta}$ | = | rate of change of sideslip angle |
| $\phi$, $\theta$, $\psi$ | = | roll, pitch and heading angles |
| $\rho$ | = | density of air |
| $\nu$ | = | kinematic viscosity |
| $\omega$ | = | angular rates $[\ p\ q\ r\ ]^T$ |

*Subscripts*

| | | |
|---|---|---|
| $ac$ | = | aircraft |
| $b$ | = | body-fixed frame |
| $E$ | = | Earth-fixed axis system |
| $f$ | = | due to fuselage |
| $G$ | = | due to gravity |
| $h$ | = | horizontal tail |
| $w$ | = | wing |
| $x$, $y$, $z$ | = | body-fixed axis system directions |
| $\alpha$, $\beta$ | = | derivative per angle of attack or sideslip angle |

# I. Introduction

MAVs have become increasingly popular in military and commercial application.[1] Challenges in MAV design stem in part from the lack of aerodynamic data and the inability to accurately estimate aerodynamic performance at low Reynolds numbers. The complexity of low Reynolds number flow can be observed from the results of wind tunnel studies of airfoils and wings at Reynolds numbers below 500,000.[2–9] Spedding and McArthur[10] showed that the span efficiency factors for an airfoil and wing at low Reynolds numbers deviated significantly from those at higher Reynolds numbers. The goal of this study was to use an off-board motion tracking system to obtain flight data at low Reynolds number regimes at which MAVs operate. These data would contribute to help better understand the aerodynamic performance of slow flying, fixed-wing MAVs.

Free-flight tests can aid in the measurement of aerodynamic characteristics of MAVs. Owing to the small size and weight of MAVs, it is difficult to mount on-board sensors without altering the aerodynamic and handling characteristics of the aircraft. Thus, state-of-the-art motion tracking techniques can be used to obtain flight data and determine the aerodynamic performance of MAVs.[11–18]

Extensive research has been conducted in the design and testing of low-cost, high-performance propellers for MAVs.[19,20] However, the use of propellers in aircraft propulsion results in the interaction between the propeller wake and aerodynamic surfaces of the aircraft. This interaction can affect the aerodynamic performance of the aircraft. Several wind tunnel and numerical studies have been dedicated to investigating the influence of propeller wake on the aerodynamic performance of a wing.[21–24]

In the current research, a commercially manufactured Extra 300 3D and a custom-built Extra 260 were used to gather flight test data using a 16 camera motion tracking system. The lift and drag characteristics of both aircraft were obtained for free-flight conditions. In addition to glide flight results for both aircraft, the Extra 300 3D was tested with the propeller operating over a range of advance ratios. A commercially manufactured E-flite™ propeller was mounted on the nose of the Extra 300 3D aircraft. As no experimental data were available for the propeller, a thrust model based on the blade element theory was developed and implemented. It was critical to develop a model that closely resembled the propeller behavior in order to better predict the aerodynamic performance of the aircraft at various propeller speeds and advance ratios.

This paper presents experimentally determined lift and drag characteristics for the Extra 260 and Extra 300 3D in free flight. The test aircraft flew at a nominal Reynolds number of approximately 25,000 based on the wing mean aerodynamic chord. The results for the complete airframe show the aerodynamic


Copyright © 2012 by the author. Published by the American Institute of Aeronautics and Astronautics, Inc., with permission.

**Figure 1. Motion tracking facility using the Vicon system at UIUC.**

characteristics of the MAVs over a range of angles of attack. Results in the glide flight regime are compared with theory, and results from powered flight are presented to show the influence of propeller slipstream on the aerodynamic characteristics of the Extra 300 3D.

## II. Experimental Apparatus

### A. Laboratory Setup

Figure 1 shows the motion tracking facility at UIUC. Sixteen cameras, each with its own infrared light source, were used by the Vicon motion tracking system. Reflective markers [approximately 5-mm (0.2-in) diameter] were attached to the surface of the aircraft to generate strong point reflections. The cameras tracked the circular reflections in their field of view, and using multiple camera views, the Vicon software triangulated the reflections in three dimensions. The Vicon software returns both position and orientation of the airplane in the Earth-referenced frame, and these data were analyzed to obtain velocities and acceleration in the body-fixed frame. Each part of the aircraft (fuselage, propeller, etc.) was tracked as an individual object. A recording rate of 200 Hz was used to capture the tracking data.

### B. Extra 260 and Extra 300 3D

Figure 2 shows the top and side views of a model of the scaled aerobatic Extra 260[25] aircraft that was custom-built for use with the motion tracking system. The "profile"-type aircraft was produced from 2-mm depron foam sheets using a high precision laser cutter. The aircraft had a wingspan of 41.27 cm (16.25 in), length of 39.37 cm (15.50 in) and weight of 33.62 g (1.18 oz).

The primary airframe and control surfaces were supported by carbon fiber rods. Carbon pushrods that were connected to the miniature servos enabled the actuation of the ailerons, elevator, and rudder. A 3.7-V battery was used to power a receiver that controlled the servos of the aircraft. The geometric properties for the aircraft are listed in Table 1.

The second aircraft tested was a 32-g (1.13-oz) Extra 300 3D, as shown in Fig. 3.[26] The aircraft had a


Copyright © 2012 by the author. Published by the American Institute of Aeronautics and Astronautics, Inc., with permission.

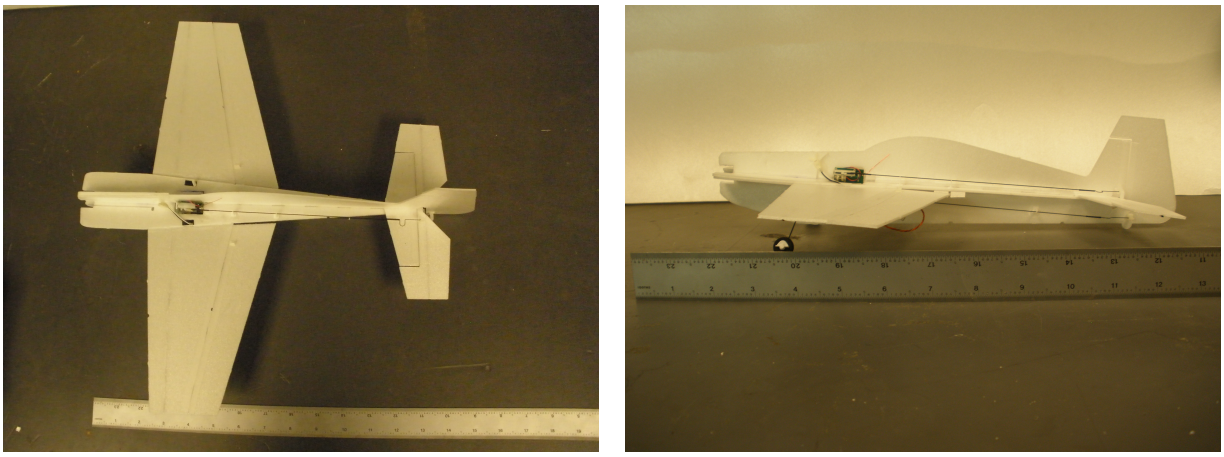

(a) Top view of the Extra 260 .

(b) Side view of the Extra 260.

**Figure 2. Scaled model of Extra 260.**

**Table 1. Geometric Properties of the Extra 260**

| | | |
|---|---|---|
| Mass | 33.62 g | (1.18 oz) |
| Wingspan | 41.27 cm | (16.25 in) |
| Wing area ($S_{\mathrm{w}}$) | 403.1 cm$^2$ | (62.48 in$^2$) |
| Wing chord (at root) | 13.0 cm | (5.13 in) |
| Reference area ($S_{ref}$) | 472.1 cm$^2$ | (73.18 in$^2$) |
| Length | 39.37 cm | (15.50 in) |
| Horizontal tail area ($S_h$) | 102.7 cm$^2$ | (15.93 in$^2$) |
| Vertical tail area | 54.56 cm$^2$ | (8.45 in$^2$) |

wingspan of 42.67 cm (16.8 in) and an overall length of 49.27 cm (19.4 in). As shown in Fig. 3, the airframe was constructed from depron foam and comprised of carbon fiber wing struts. From the top and side views of the Extra 300 3D (see Fig. 3), it can be seen that cut outs were made in the depron foam to reduce the weight of the primary airframe and control surfaces without comprising on the structural integrity of the aircraft. A thin plastic film was stretched over the top of the wing and tail structures to form membrane aerodynamic surfaces. Thrust was generated by an electric motor driving a propeller with a diameter of 13 cm (5.12 in) and a pitch of 7 cm/rev (2.75 in/rev). The geometric properties of the Extra 300 3D are listed in Table 2.

## III. Method of Data Acquisition

The method of data acquisition is similar to that used in earlier research.[17,18,27] Each part of the aircraft (fuselage, propeller, etc.) was tracked as an individual object. The data stream provided by the Vicon system included the Earth-referenced position and the Euler angles for each of the objects. The tracking system provided information on whether the object was visible to the camera system and if it was, the attitude and position of the object. Motion track data for each object was filtered to acquire useful measurements.

For trajectory of the fuselage object, the position and attitude were used in the post processing to determine the angular rate, angular acceleration, translation velocity, and translational acceleration of the airplane. The first step was to transform the raw measured data from object-fixed reference frame as recorded by the tracking system to the center of gravity of the airplane. The body-fixed frame is the standard aircraft reference frame defined with $x$ out the nose and $y$ out the right wing. By measuring the distance and rotation between the airplane center of gravity and the object-fixed origin, the rotation offset between the two frames was known. A transformation matrix was used to combine the measured rotational offset and


Copyright © 2012 by the author. Published by the American Institute of Aeronautics and Astronautics, Inc., with permission.

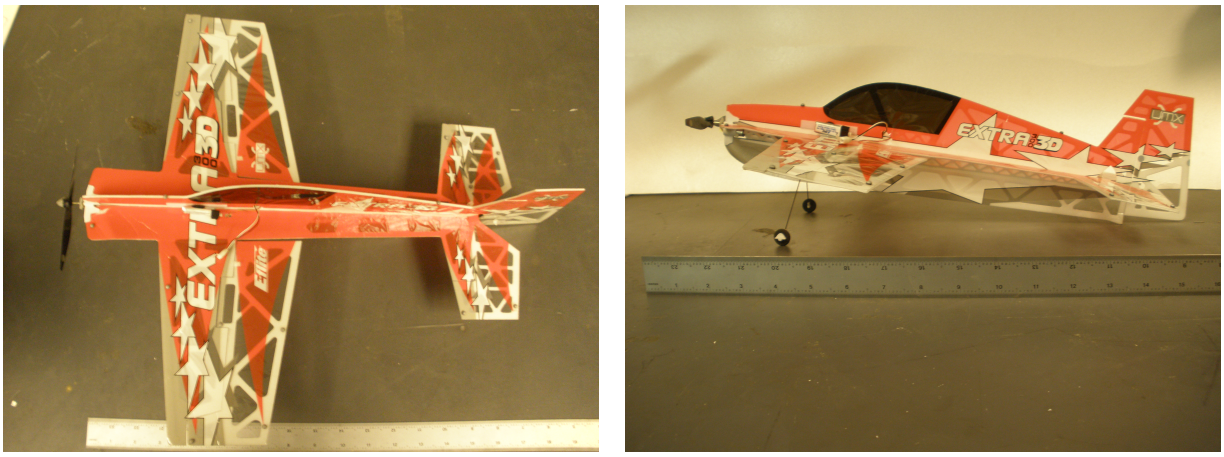

(a) Top view of the Extra 300 3D. (b) Side view of the Extra 300 3D.

**Figure 3. Commercially manufactured Extra 300 3D.**

**Table 2. Geometric Properties of the Extra 300 3D**

| | | |
|---|---|---|
| Mass | 32.00 g | (1.13 oz) |
| Wingspan | 42.67 cm | (16.80 in) |
| Wing area ($S_{\mathrm{w}}$) | 467.4 cm$^2$ | (72.45 in$^2$) |
| Wing chord (at root) | 13.3 cm | (5.25 in) |
| Reference area ($S_{ref}$) | 571.9 cm$^2$ | (88.66 in$^2$) |
| Length | 49.27 cm | (19.40 in) |
| Horizontal tail area ($S_h$) | 159.6 cm$^2$ | (24.75 in$^2$) |
| Vertical tail area | 75.35 cm$^2$ | (11.68 in$^2$) |

the Earth-referenced tracking data. In order to rotate between different axis systems, the standard rotation matrix depending on the three Euler angles($\phi$, $\theta$ and $\psi$) was used, viz

$$\mathbf{R} = \begin{bmatrix} \cos\theta\cos\psi & \cos\theta\sin\psi & -\sin\theta \\ \sin\phi\sin\theta\cos\psi - \cos\phi\sin\psi & \sin\phi\sin\theta\sin\psi - \cos\phi\cos\psi & \sin\phi\cos\theta \\ \cos\phi\sin\theta\cos\psi - \sin\phi\sin\psi & \cos\phi\sin\theta\sin\psi - \sin\phi\cos\psi & \cos\phi\cos\theta \end{bmatrix} \tag{1}$$

A matrix was first developed for the transformation from the airplane object measurement frame to the airplane center of gravity body-fixed frame. The resulting matrix was labeled $\mathbf{R}_{measured\ to\ CG}$. The second transformation matrix, $\mathbf{R}_{inertial\ frame}$, was from the Earth-fixed inertial reference frame to the tracking object center and was recorded at each time step. By combining these two rotations through the multiplication of $\mathbf{R}_{measured\ to\ CG}$ and $\mathbf{R}_{inertial\ frame}$, the transformation from the Earth-fixed reference frame to the airplane center of gravity was calculated by

$$\mathbf{R}_{earth\ to\ body} = \mathbf{R}_{measured\ to\ CG} \cdot \mathbf{R}_{inertial\ frame} \tag{2}$$

From the resulting $\mathbf{R}_{earth\ to\ body}$ matrix, the Earth-referenced attitude at the airplane center of gravity were determined by calculating $\theta$, $\phi$, and $\psi$ as well as $x$, $y$, and $z$.

In post processing, the voids where the system was unable to triangulate the MAV were located and were estimated using linear interpolation based on the neighboring points in the trajectory time history. After filling in these points that represented less than 0.7% of the time history, the raw measurements were smoothed using a third-order polynomial regression (Savitzky-Golay) method.[28] The first and second derivatives of the Earth-referenced position and attitude time histories were also calculated by the algorithm during the smoothing process. The polynomial regression results were used to determine the forces and moments acting on the airplane in the body-fixed frame.


Copyright © 2012 by the author. Published by the American Institute of Aeronautics and Astronautics, Inc., with permission.

### A. Lift and Drag Measurement

From the smoothed and differentiated data, the position of the airplane along with the velocity and acceleration in the Earth-referenced frame as well as the Euler angles were known. To transform these quantities into a body-fixed reference frame, a rotation matrix (Eq. 1) based on the Euler angles was used.[16,29] First, the velocity and acceleration were transformed from the Earth-referenced frame to the body-fixed frame along with an offset vector $\mathbf{r}$ using

$$\mathbf{V}_b = [\ u\ v\ w\ ]^T \quad = \mathbf{R}_{earth\ to\ body}\ \ [\ \dot{x}_E\ \dot{y}_E\ \dot{z}_E\ ]^T + (\boldsymbol{\omega} \times \mathbf{r}) \tag{3a}$$

$$\mathbf{a}_b = [\ a_x\ a_y\ a_z\ ]^T = \mathbf{R}_{earth\ to\ body}\ \ [\ \ddot{x}_E\ \ddot{y}_E\ \ddot{z}_E\ ]^T + \dot{\boldsymbol{\omega}} \times \boldsymbol{r} + \boldsymbol{\omega} \times (\boldsymbol{\omega} \times \mathbf{r}) \tag{3b}$$

to obtain body-fixed axes velocity $\mathbf{V}_b$ and acceleration $\mathbf{a}_b$. The offset vector $\mathbf{r}$ is the distance from the origin of the body-fixed frame to the tracked object-fixed frame. The angular rates were calculated by transforming the Euler angular rates to the body-fixed angular rates using[16,30]

$$\begin{bmatrix} p \\ q \\ r \end{bmatrix} = \begin{bmatrix} 1 & 0 & -\sin\theta \\ 0 & \cos\phi & \sin\phi\cos\theta \\ 0 & -\sin\phi & \cos\phi\cos\theta \end{bmatrix} \begin{bmatrix} \dot{\phi} \\ \dot{\theta} \\ \dot{\psi} \end{bmatrix} \tag{4}$$

From the three components of velocity [see Eq. 3(a)], the total inertial speed $V$ could be calculated from

$$V = \sqrt{u^2 + v^2 + w^2} \tag{5}$$

With all of these quantities known over the duration the flight, the analysis of the aerodynamic performance was completed. To obtain the angle of attack and sideslip angle, the measured inertial speed $V$ can be used if two assumptions are made. First, the air mass is assumed to be quiescent, and second the induced flow effects on the aircraft are negligible. With these assumptions, the freestream flow angles were found from

$$\alpha = \tan^{-1}(w/u) \tag{6a}$$

$$\beta = \sin^{-1}(v/V) \tag{6b}$$

The forces acting on the airplane were known since the mass of the airplane was fixed, and the body-fixed axes accelerations ($a_x$, $a_y$, $a_z$) were known from the position tracking data. The total external forces acting on the airplane were calculated from the expression

$$\mathbf{F}_{external} = [\ a_x\ a_y\ a_z\ ]^T\ m \tag{7}$$

By subtracting the force of gravity $\mathbf{F}_G$ and thrust force $\mathbf{F}_T$ from the total external forces, the aerodynamic forces acting on the airplane were determined from

$$\mathbf{F}_{aero} = \mathbf{F}_{external} - \mathbf{F}_G - \mathbf{F}_T \tag{8}$$

where $\mathbf{F}_G$ is given by

$$\mathbf{F}_G = mg\ [-\sin\theta\ \ \sin\phi\cos\theta\ \ \cos\phi\cos\theta]^T \tag{9}$$

Three resulting components ($F_x$, $F_y$, $F_z$) of the aerodynamic force $\mathbf{F}_{aero}$ were in the body-fixed axes frame. To calculate lift and drag, which are the force components in the wind axes, the forces in the body frame were transformed into the wind frame using

$$L = -F_z\cos\alpha + F_x\sin\alpha \tag{10a}$$

$$D = -F_z\sin\alpha\cos\beta - F_x\cos\beta\cos\alpha - F_y\sin\beta \tag{10b}$$

By not making a small angle approximation on the sideslip angle $\beta$ in the drag calculations, the result was more accurate for a maneuvering aircraft. The angle of attack and sideslip angle were calculated throughout the flight to understand the performance of the aircraft.


Copyright © 2012 by the author. Published by the American Institute of Aeronautics and Astronautics, Inc., with permission.

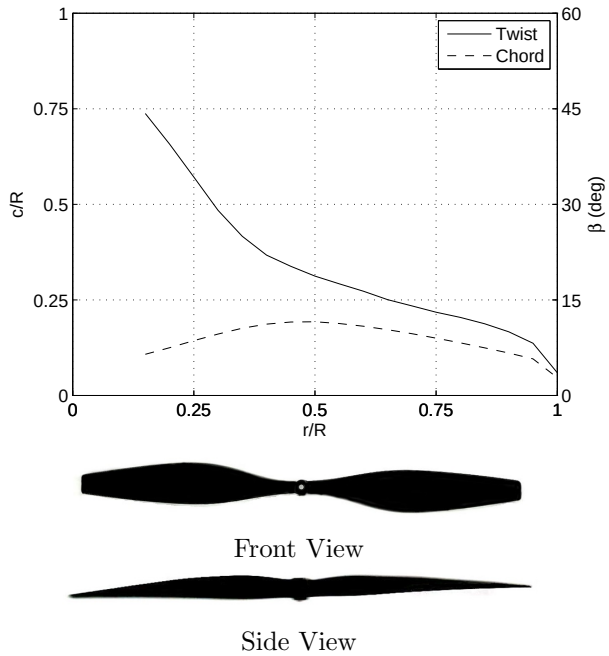


**Figure 4. Geometric characteristics of the E-flite propeller.**

## B. Thrust Measurement

A commercially manufactured E-flite propeller (see Fig. 4) was used in the current study. The rotational speed of the propeller was calculated using the attitude time history of the propeller object. The propeller object was tracked using flat markers made of reflective tape elements that were placed on the hub and blades of the propeller. Tracking the propeller proved to be more challenging to the motion tracking system than slow moving objects, and this resulted in more voids in the propeller trajectory than the fuselage (aircraft) trajectory. Despite using fast sampling rates (above the Nyquist frequency), there could be as few as two measurements during each rotation of the propeller.

In order to overcome these challenges, the attitude time history of the propeller was represented by quaternions. The quaternions were used for calculating the angular change in propeller attitude between two sequential measurements ($q_1$ and $q_2$) using[31]

$$\delta = 2\cos^{-1}(q_1 \cdot q_2) \tag{11}$$

After calculating the angular change in propeller attitude, the rotational speed was determined from

$$n = \frac{\delta}{2\pi dt} \tag{12}$$

where $dt$ was the time interval between measurements.

## C. Thrust Model Development

Experimentally measured thrust at various advance ratios were not available for the propeller. Thus, the propeller thrust was modeled using the blade element theory.[32] The twist and chord distributions of the propeller were determined using the PropellerScanner software.[33] The program used the front and side views of the propeller as shown in Fig. 4 to estimate the twist and chord distribution, the results of which are shown in Fig. 4. Following the determination of the twist and chord distribution, the thrust coefficient $C_T$ of the propeller was predicted. Figure 5 shows the thrust coefficient $C_T$ of the propeller as a function of advance ratio $J$. With this data, the thrust coefficient was estimated at each flight data point using the instantaneous advance ratio, that is

$$J = \frac{V}{nD_p} \tag{13}$$


Copyright © 2012 by the author. Published by the American Institute of Aeronautics and Astronautics, Inc., with permission.

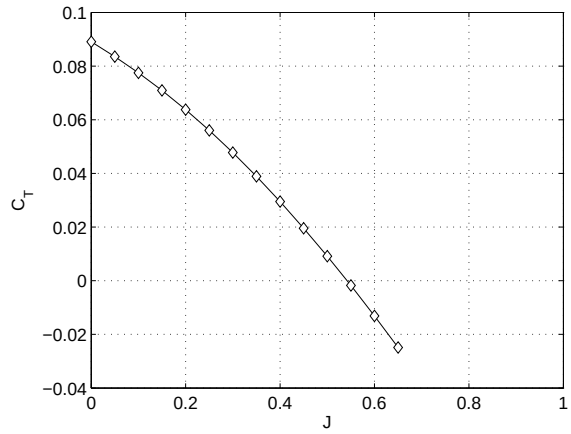


**Figure 5. Thrust characteristics of the Extra 300 3D propeller.**

where $V$ is the airspeed, $n$ is the rotational speed in revolutions per second (Eq. 12) and $D_p$ is the diameter of the propeller. From the thrust coefficient, the thrust force of the propeller is given by

$$T = \rho n^2 {D_p}^4 C_T \tag{14}$$

The propeller and hence the thrust force was aligned with the body-fixed $x$ axis so that the thrust force vector $F_T$ was estimated to have thrust $T$ in the $x$ direction. By using the motion tracking system to determine the propeller speed and forward velocity, results from blade element theory were used to estimate the propeller thrust throughout flight at varying advance ratios.

# IV. Results and Discussion

In this section, the aerodynamic characteristics of the Extra 260 and Extra 300 3D in glide flight as well as results from the powered flight tests of the Extra 300 3D are presented.

## A. Unpowered Flight Tests

### *1. Lift and Drag Characteristics*

The lift and drag characteristics of the Extra 260 and Extra 300 3D during hand-launched glide flights are presented in Figs. 6 and 7. The results shown in Figs. 6 and 7 correspond to conditionally-sampled low angular rate data ($<$ 30 deg/sec) with a least-squares parabolic fit to the drag polar and a linear fit to the lift curve. By limiting the angular rates, unsteady flight dynamics effects could be minimized.[18]

A parabolic fit was applied to the low angular rate data shown in the drag polars of Figs. 6 and 7. The parabolic fit is of the standard form given by

$$C_D = C_{D_o} + KC_L^2 \tag{15}$$

where $C_{D_o}$ is the parasite drag and $KC_L^2$ is the induced drag due to lift where

$$K = \frac{1}{\pi e_o \mathcal{A}R} \tag{16}$$

In Eq. 16, $e_o$ is the Oswald efficiency factor.[32] The resulting curve fits for the Extra 260 and Extra 300 3D are given by

$$C_D = 0.0554 + 0.5278C_L^2 \tag{17}$$

$$C_D = 0.1015 + 0.5349C_L^2 \tag{18}$$

From Eqs. 17 and 18, it is observed that the $C_{D_o}$ values for the Extra 260 and Extra 300 3D are 0.0554 and 0.1015, respectively. It should be noted that in both cases the parasite drag include the additive drag


Copyright © 2012 by the author. Published by the American Institute of Aeronautics and Astronautics, Inc., with permission.

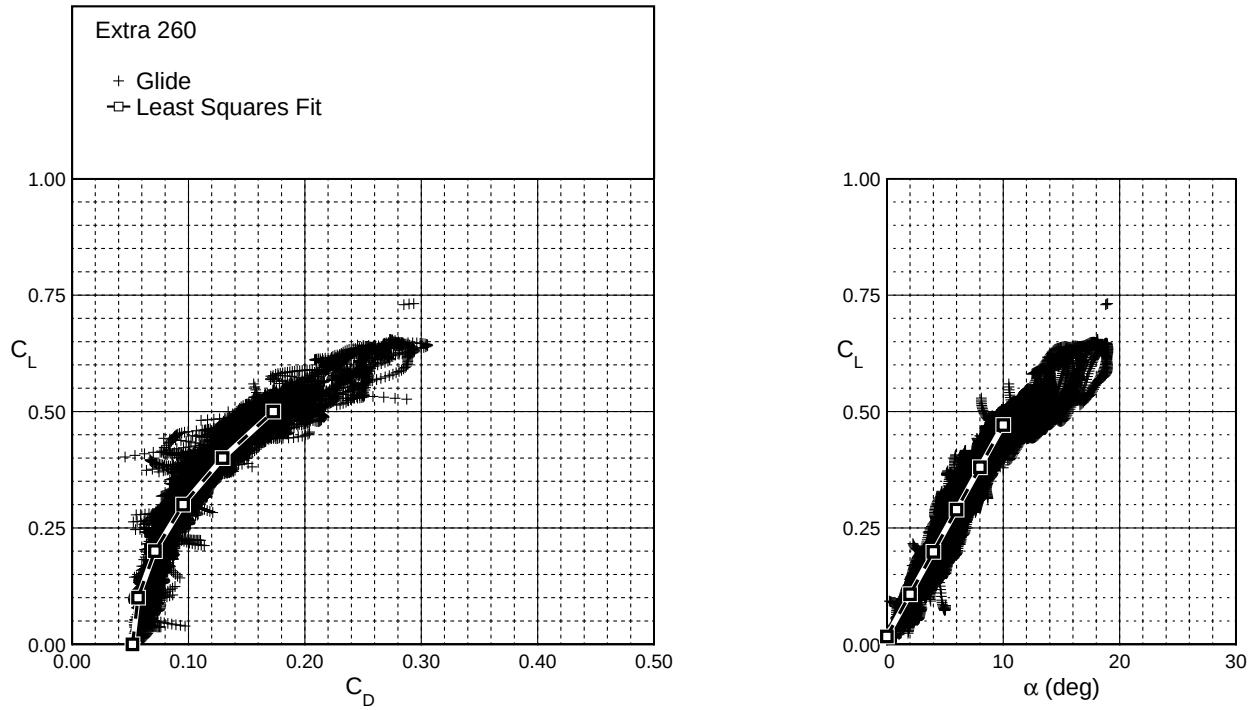


**Figure 6. Experimentally determined drag polar and lift curve for the Extra 260.**

due to the reflective markers (approximately eight per aircraft). The Extra 300 3D has a higher $C_{D_o}$ owing in part to the drag of the unpowered (static) propeller. Also, the Extra 300 3D had covering applied to only one side of the depron foam thereby leaving the sharp edges of the cutouts exposed, which produced additional drag.

The lift of the entire MAV depends on both the wing and horizontal tail,[34] viz

$$C_L = C_{L_w} + C_{L_h}\eta_h \frac{S_h}{S_{ref}} \tag{19}$$

where $\eta_h$ is the dynamic pressure ratio at the tail and taken to be 0.9. The reference area ($S_{ref}$) and horizontal tail area ($S_h$) for the two aircraft are given in Tables 1 and 2. The pitching moment $C_{M_{cg}}$ is given by

$$C_{M_{cg}} = C_{M_{ac,w}} + C_{L_w}(\overline{x}_{cg} - \overline{x}_{ac,w}) - C_{L_h}\eta_h \frac{S_h}{S_{ref}}(\overline{x}_{ac,h} - \overline{x}_{cg}) \tag{20}$$

where the center of gravity $\overline{x}_{cg}$ was measured to be 32% and 38% of the wing root chords of the Extra 260 and Extra 300 3D, respectively. The pitching moment of the wing $C_{M_{ac,w}}$ was taken as zero, and the aerodynamic center of the wing $\overline{x}_{ac,w}$ and the tail $\overline{x}_{ac,h}$ were approximated to be located at 25% of the respective mean aerodynamic chord. During flight, $C_{M_{cg}}$ and $C_L$ for the airplane were determined from the flight trajectory.

In Eqs. 19 and 20, the only remaining unknown parameters are the wing $C_{L_w}$ and the tail $C_{L_h}$. Solving the two equations simultaneously results in

$$C_{L_h} = \frac{C_{M_{ac,w}} - C_{M_{cg}} + C_L(\overline{x}_{cg} - \overline{x}_{ac,w})}{\frac{S_h}{S_{ref}}\eta_h(\overline{x}_{ac,h} - \overline{x}_{ac,w})} \tag{21a}$$

$$C_{L_w} = \frac{C_{M_{cg}} - C_{M_{ac,w}} + C_L(\overline{x}_{ac,h} - \overline{x}_{cg})}{(\overline{x}_{ac,h} - \overline{x}_{ac,w})} \tag{21b}$$

From the glide flight measurements, the trim flight condition for a set of flights was found using the following method. First, the trim angle of attack $\alpha_{trim}$ for each flight was found using a linear least-squares fit to find $C_{M_o}$ and $C_{M_\alpha}$ in the form

$$C_{M_{cg}} = C_{M_o} + C_{M_\alpha}\alpha \tag{22}$$


Copyright © 2012 by the author. Published by the American Institute of Aeronautics and Astronautics, Inc., with permission.

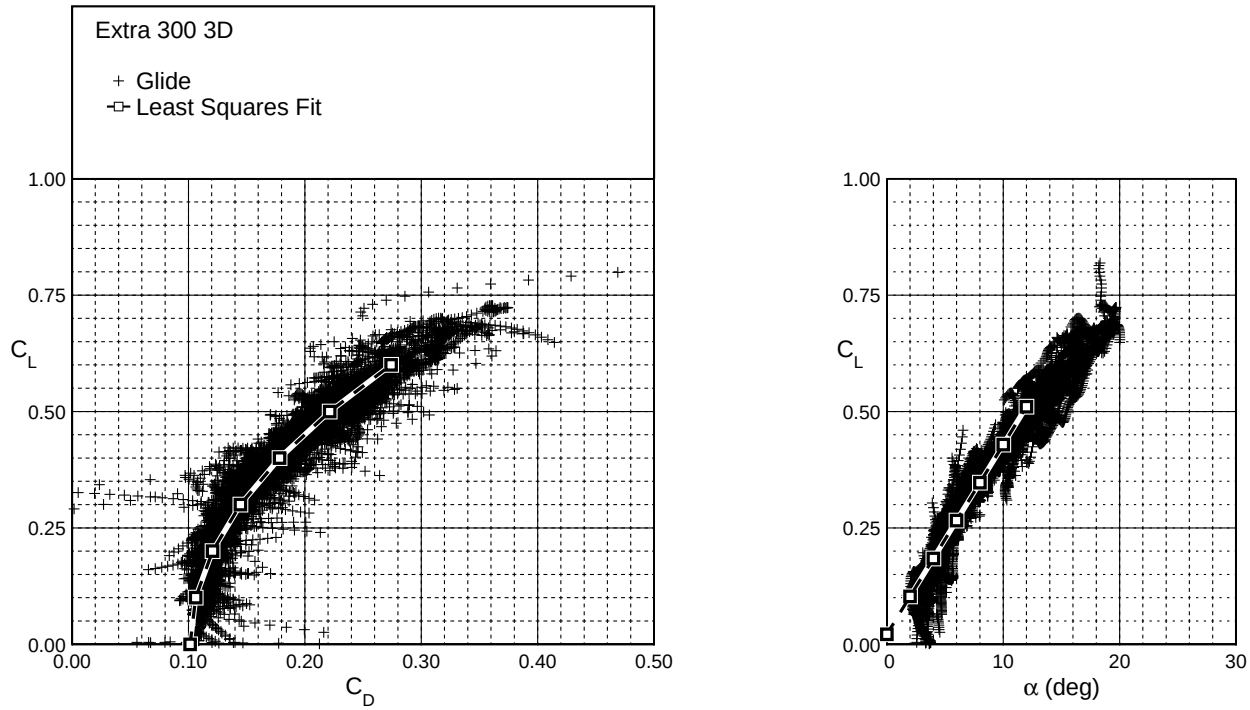


**Figure 7. Experimentally determined drag polar and lift curve for the Extra 300 3D.**

Taking $C_{M_{cg}} = 0$ yields the trim angle of attack $\alpha_{trim}$. Next, a fit was used to determine $C_L$ as a function of angle of attack in the form

$$C_L = C_{L_o} + C_{L_\alpha}\alpha \tag{23}$$

With both $C_{L_o}$ and $C_{L_\alpha}$ known for a set of flights, $C_{L_{trim}}$ was calculated by evaluating Eq. 23 at $\alpha_{trim}$ found previously. The result is a trim lift coefficient for each set of flights that can be used in Eq. 21(b) to yield the wing lift coefficient $C_{L_w}$.

At each trim point, Eq. 21(b) was used with $C_{M_{cg}} = 0$ and $C_L$ to find $C_{L_w}$. Figure 8 shows the trim $C_L$ for the entire aircraft and the corresponding lift coefficient of just the wing $C_{L_w}$ as a function of the angle of attack during glide flights of the Extra 260. For comparison, Fig. 8 also includes the previously discussed conditionally-sampled low angular rate data. Figure 9 shows $C_L$ for the entire aircraft and $C_{L_w}$ from Eq. 21(b) for the conditionally-sampled flight data (previously shown in Fig. 6). A linear fit was used to determine the lift curve slope for both cases. The lift curve slope for the entire aircraft is 2.60/rad, and the lift curve slope for the wing alone is 2.11/rad (see Fig. 9).

For the Extra 300 3D, Fig. 10 shows the trim $C_L$ for the entire aircraft and the corresponding lift coefficient of just the wing $C_{L_w}$ as a function of the angle of attack during glide flights. Figure 11 shows $C_L$ for the entire aircraft and $C_{L_w}$. A linear fit was used, and the lift curve slope of the entire aircraft and wing were found to be 2.27/rad and 2.03/rad, respectively. For both aircraft tested (Extra 260 and Extra 300 3D), the calculated lift of the wing was less than that of the entire aircraft which indicates a lifting horizontal tail.

Theoretical values of the lift curve slope were obtained from classical lifting line theory given by

$$C_{L_\alpha} = 2\pi\left(\frac{Æ}{Æ + 2}\right) \tag{24}$$

where $Æ$ is calculated from

$$Æ = \frac{b^2}{S_{ref}} \tag{25}$$

where $b$ is the wingspan and $S_{ref}$ is the reference area. From the wingspans ($b$) and reference areas ($S_{ref}$) provided in Tables 1 and 2, the aspect ratios for the Extra 260 and Extra 300 3D were calculated to be 3.60 and 3.18, respectively.


Copyright © 2012 by the author. Published by the American Institute of Aeronautics and Astronautics, Inc., with permission.

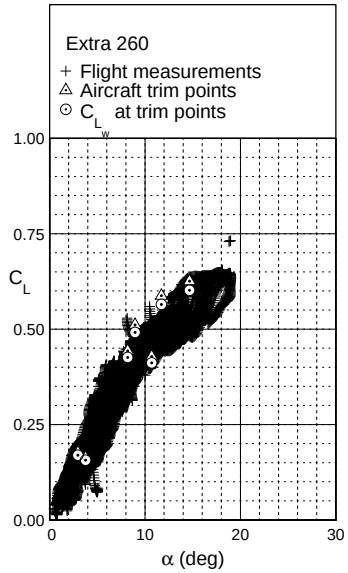


**Figure 8. Experimentally determined lift coefficients for the entire aircraft and the wing at the trim points during the conditionally-sampled flights of the Extra 260.**

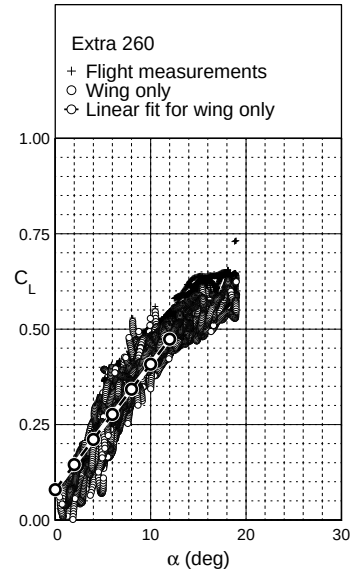


**Figure 9. Comparison of the experimentally determined lift coefficients of the entire aircraft and wing for the Extra 260.**

The experimental lift curve slope for the Extra 260 was 2.11/rad which was lower than the 4.04/rad predicted by lifting line theory (Eq. 24). A similar result was observed for the Extra 300 3D that had an experimental lift curve slope of 2.03/rad while the value obtained from lifting line theory was 3.85/rad. This decrease is not unexpected because the lift curve slope decreases for finite wings and airfoils at low Reynolds numbers.[10]

However, a reduced lift curve slope of 3.69/rad was obtained for the Extra 260 using a relation more appropriate for low $Æ$ wings, viz

$$C_{L_\alpha} = 2\pi \left( \frac{Æ}{2 + \sqrt{4 + Æ^2}} \right) \tag{26}$$

For the Extra 300 3D, using Eq. 26, the lift curve slope was calculated to 3.47/rad.

As expected, both of these results from theory (with Eq. 26 being most appropriate) over predict the lift curve slope primarily as a result of low Reynolds number effects, and this result is consistent with past measurements.[10]

## B. Powered Flight Tests

The propeller wake over the aircraft wing and fuselage has a significant impact on the lift, drag, and stability of the aircraft. A propeller produces thrust by accelerating a large mass of air rearward, and this air flows over a portion of the wing and fuselage. The total lift produced is a combination of the lift generated by the airframe area not in the wake of the propeller and the region influenced by the propeller slipstream. Thus, the lift can be altered by varying the rotational speed (RPM) of the propeller. In the current study, a commercially manufactured E-flite propeller with a diameter of 13 cm (5.12 in) and pitch of 7 cm/rev (2.75 in/rev) was mounted on the nose of the aircraft. The forces due to the propeller running at various speeds were taken into account by using the $C_T$ results previously discussed (Fig. 5). After accounting for the forces due to the running propeller, the lift and drag forces acting on the aircraft were obtained. The aerodynamic performance of the aircraft is presented for three ranges of advance ratio: low (0.30–0.45), moderate (0.45–0.60), and high (0.60–1.0).

The aerodynamic performance of the Extra 300 3D for specific ranges in advance ratio is compared with the lift and drag characteristics during glide flight. In order to make this comparison, the drag from the unpowered propeller was taken into account. The increase in aircraft drag coefficient due to a static


Copyright © 2012 by the author. Published by the American Institute of Aeronautics and Astronautics, Inc., with permission.

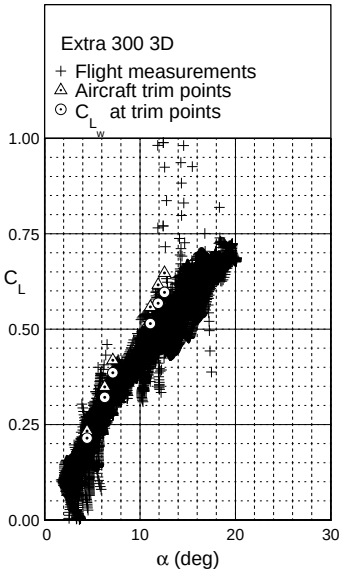


**Figure 10. Experimentally determined lift coefficients for the entire aircraft and the wing at the trim points during the conditionally-sampled flights of the Extra 300 3D.**

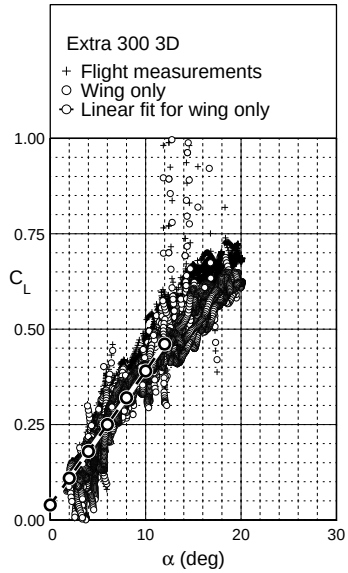


**Figure 11. Comparison of the experimentally determined lift coefficients of the entire aircraft and wing for the Extra 300 3D.**

propeller ($\Delta C_D$) is given by

$$\Delta C_D = C_{D_{FP}} \frac{S_{prop}}{S_{ref}} \tag{27}$$

where $C_{D_{FP}}$ is the drag coefficient for a flat plate, $S_{prop}$ is the frontal area of the static propeller and $S_{ref}$ is the reference area of the aircraft. From Eq. 27, $\Delta C_D$ was found to be approximately 0.034. This change in the value of $C_D$ is shown in Fig. 12. The parameter values used in Eq. 27 are given in Table 3.

Figures 13–15 show the lift and drag characteristics of the Extra 300 3D for specific advance ratio ranges, and a comparison is made with glide flight behavior (corrected for the static propeller). Glide flight behavior is used as a reference to highlight the change in aerodynamic characteristics that result from the running propeller. It is observed from lift curve in Fig. 13 that at the low $J$-range the slope of the lift curve is steeper than that for glide flight. From the lift curves in Figs. 14 and 15, it is observed that at the moderate and high $J$-ranges the lift curve becomes shallower and approaches glide flight behavior. The increased lift in the powered flight condition is a consequence of the enhanced aerodynamic performance of the wing and fuselage that are immersed in the propeller slipstream. The propeller wake increases the axial velocity of the flow over the inboard section of the wing which results in beneficial lift characteristics. The lift curve in Fig. 16 clearly shows the trend of augmented lift with decreasing $J$ (low speed flight).

The drag polars in Figs. 13–15 show a change in the aerodynamic performance of the aircraft at the specific ranges in advance ratio. It is observed from Fig. 13 that the drag is reduced at the low $J$-range when compared with glide. From the drag polars in Figs. 14 and 15, it is observed that at the moderate and high $J$-ranges the drag characteristics of the MAV approach glide flight. The departure from glide flight behavior can be observed from the drag polar in Fig. 16. This shift in the drag polars from right-to-left with decreasing $J$ could be as a result of the modification of the local angles of attack on the wing and fuselage

**Table 3. Parameters Used to Calculate the Change in Drag Coefficient**

| | | |
|---|---|---|
| Reference area ($S_{ref}$) | 571.99 cm$^2$ | (88.66 in$^2$) |
| Propeller frontal area ($S_{prop}$) | 9.74 cm$^2$ | (1.51 in$^2$) |
| Flat plate drag coefficient ($C_{D_{FP}}$) | 2.0 | |
| Drag coefficient change ($\Delta C_D$) | 0.034 | |


Copyright © 2012 by the author. Published by the American Institute of Aeronautics and Astronautics, Inc., with permission.

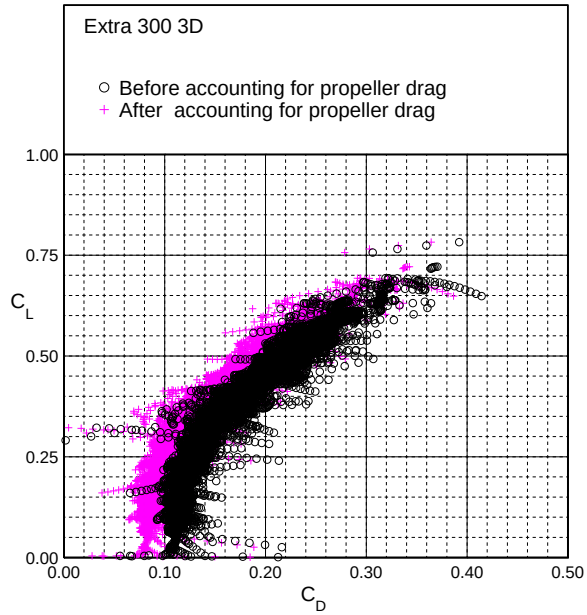


**Figure 12. Drag characteristics of Extra 300 3D before and after accounting for static propeller drag (propeller drag is subtracted).**

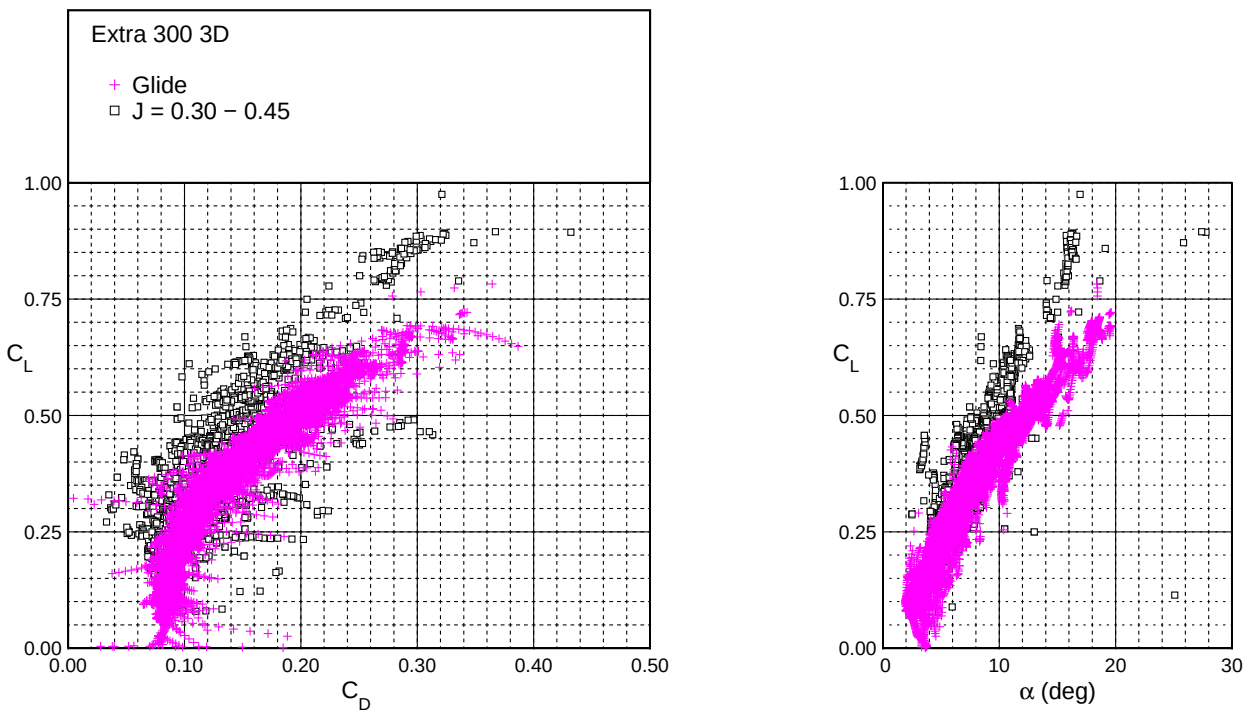


**Figure 13. Comparison of experimentally determined drag polar and lift curve for the Extra 300 3D in glide and powered flight at $J = 0.30$–$0.45$.**

by the tangential velocity in the propeller slipstream. The propeller slipstream energizes the boundary layer and promotes attached flow and thereby results in lower drag.


Copyright © 2012 by the author. Published by the American Institute of Aeronautics and Astronautics, Inc., with permission.

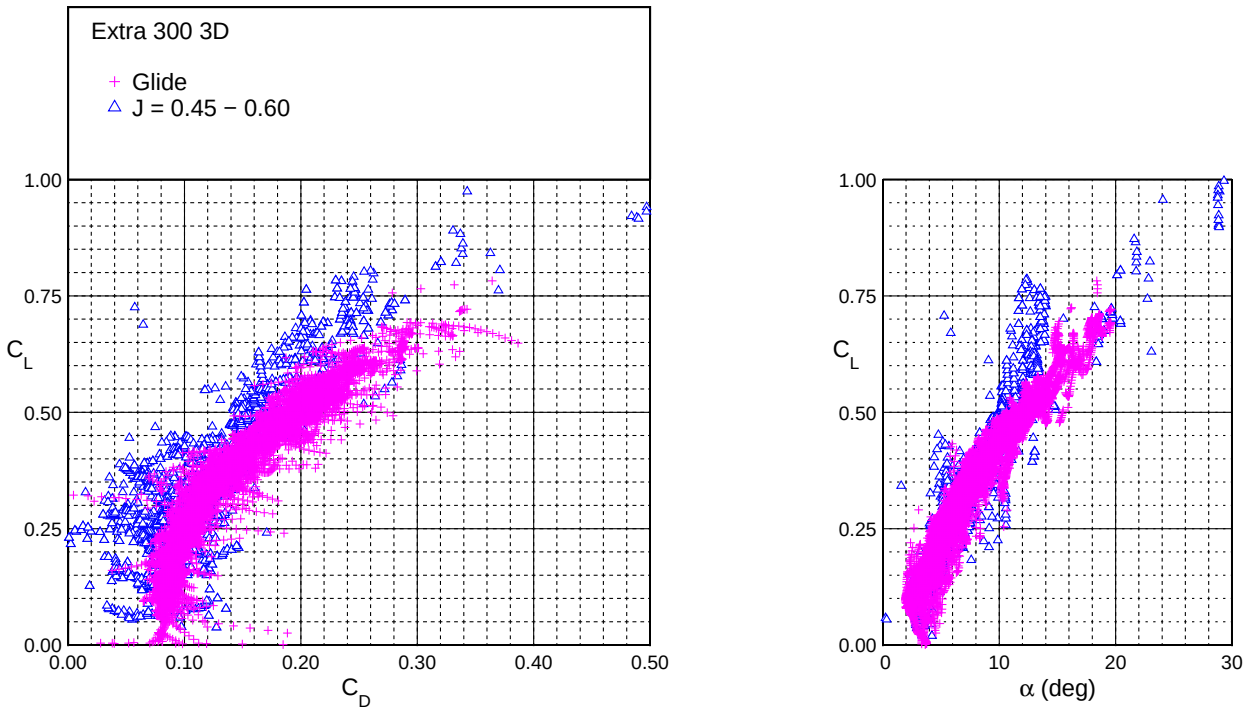


**Figure 14. Comparison of experimentally determined drag polar and lift curve for the Extra 300 3D in glide and powered flight at $J = 0.45$–$0.60$.**

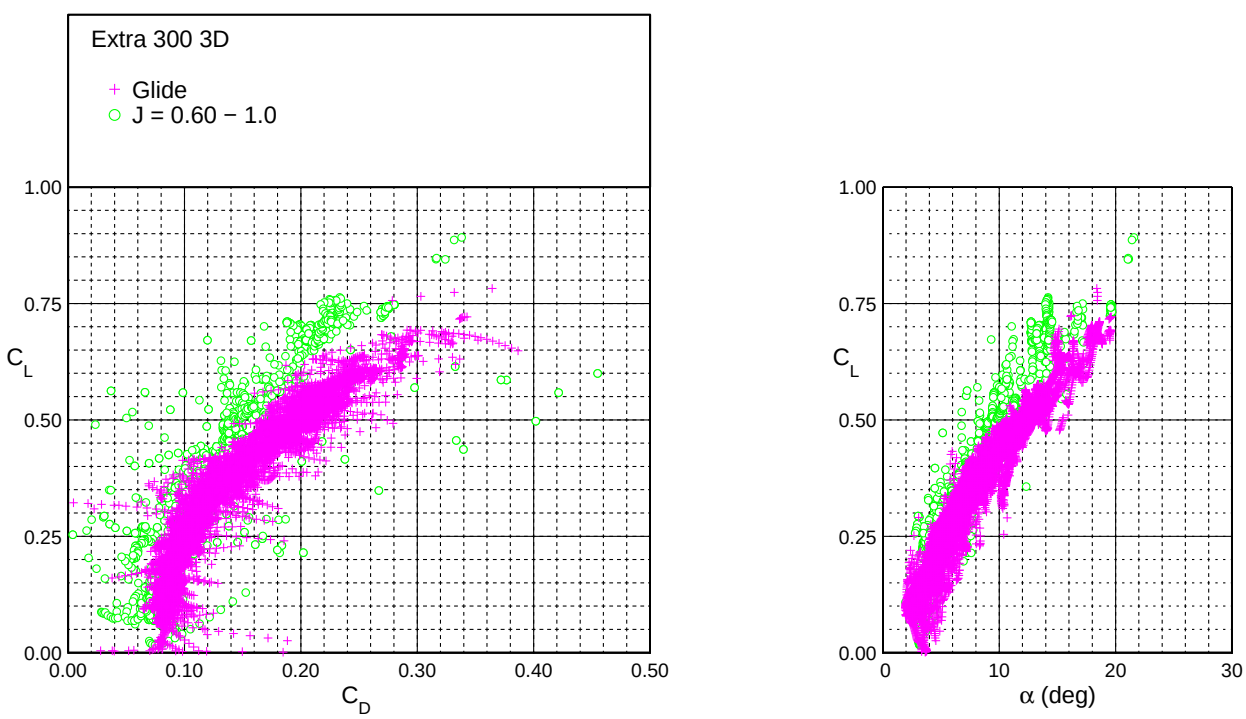


**Figure 15. Comparison of experimentally determined drag polar and lift curve for the Extra 300 3D in glide and powered flight at $J = 0.60$–$1.0$.**


Copyright © 2012 by the author. Published by the American Institute of Aeronautics and Astronautics, Inc., with permission.

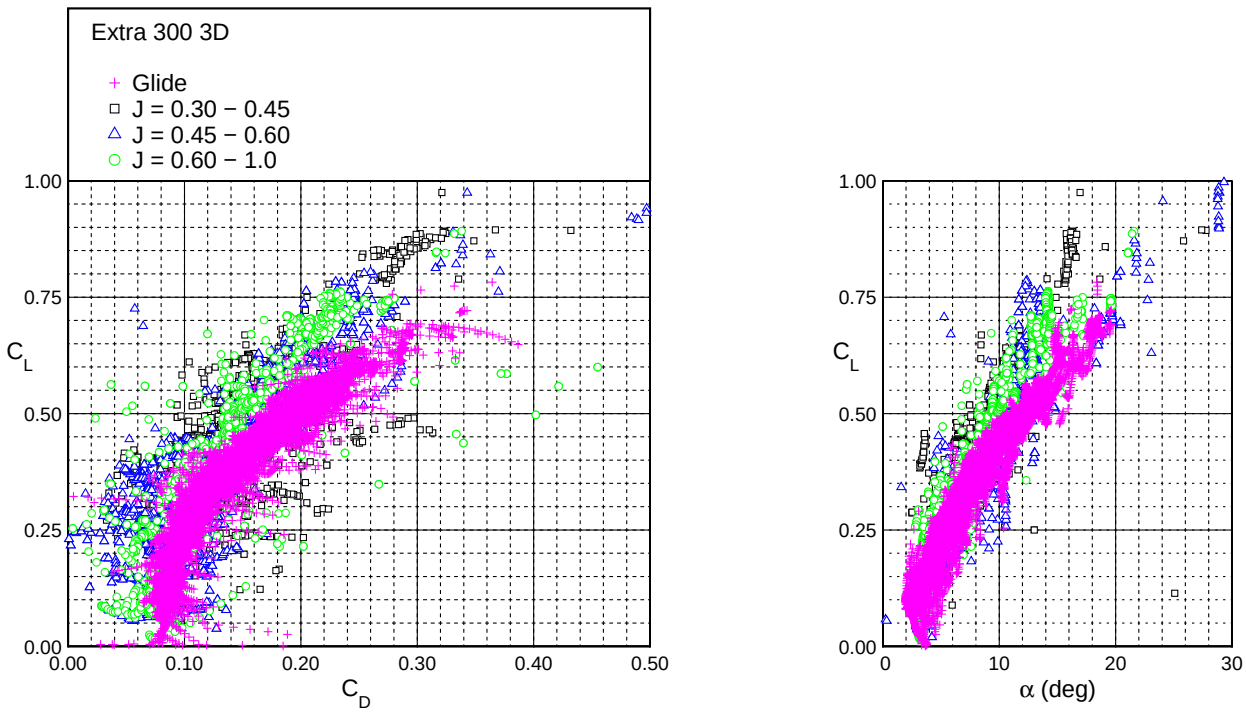


**Figure 16. Comparison of experimentally determined drag polar and lift curve for the Extra 300 3D in glide and powered flight at various ranges in advance ratio $J$.**


Copyright © 2012 by the author. Published by the American Institute of Aeronautics and Astronautics, Inc., with permission.

# V. Summary and Conclusions

The goal of this research was to obtain accurate aerodynamic data to aid in understanding the behavior of fixed-wing MAVs. Position and attitude time histories of two MAVs were obtained from a motion tracking system and used to determine the longitudinal aerodynamic characteristics in glide and powered flight. Lift and drag characteristics of the Extra 260 and Extra 300 3D were obtained for unpowered flight. For glide flight, the aerodynamics followed the expected low Reynolds number behavior with an almost linear lift curve up to stall and a drag polar that was well captured by a parabolic drag polar fit. A trim analysis was conducted to obtain the lift from the wing and thus, the resulting lift curve slope. Comparison of the experimental lift curve slope with the theoretical calculations showed that the latter over predicted the lift curve slope. These results provided useful information regarding the aerodynamics of MAVs in glide flight.

Powered flight tests were conducted for the Extra 300 3D with the propeller running at various speeds. A thrust model was implemented to aid in the accurate calculation of the lift and drag forces for specific ranges in advance ratio $J$. The results indicated that the propeller slipstream over the wing and fuselage has a beneficial effect on the aerodynamic performance that includes an increase in the lift curve slope and a reduction in drag with a decrease in the propeller advance ratio.

# VI. Acknowledgments

The authors would like to thank Geoffrey Clarkson for assisting in the use of the laser cutter and acknowledge the contributions of Gavin K. Ananda and Shreyas Narsipur in helping build the aircraft models. Also, the authors are grateful for the cooperation of Greg Milner during the course of the experiment. Finally, the authors would like to thank the UIUC Aerospace Robotics and Control Group for sharing the testing resources used in this research.

# References

[1]Pines, D. and Bohorquez, F., "Challenges Facing Future Micro-Air-Vehicle Development," *Journal of Aircraft*, Vol. 43, No. 2, March 2006, pp. 290–305.

[2]Selig, M. S., Guglielmo, J. J., Broeren, A. P., and Giguère, P., *Summary of Low-Speed Airfoil Data*, Vol. 1, SoarTech Publications, Virginia Beach, VA, 1995.

[3]Selig, M. S., Lyon, C. A., Giguère, P., Ninham, C. N., and Guglielmo, J. J., *Summary of Low-Speed Airfoil Data*, Vol. 2, SoarTech Publications, Virginia Beach, VA, 1996.

[4]Lyon, C. A., Broeren, A. P., Giguère, P., Gopalarathnam, A., and Selig, M. S., *Summary of Low-Speed Airfoil Data*, Vol. 3, SoarTech Publications, Virginia Beach, VA, 1998.

[5]Selig, M. S. and McGranahan, B. D., *Wind Tunnel Aerodynamic Tests of Six Airfoils for Use on Small Wind Turbines*, National Renewable Energy Laboratory/SR-500-34515, Golden, CO, October 2004.

[6]Laitone, E. V., "Wind Tunnel Tests of Wings at Reynolds Numbers below 70,000," *Experiments in Fluids*, Vol. 23, 1997, pp. 405–409.

[7]Pelletier, A. and Mueller, T. J., "Low Reynolds Number Aerodynamics of Low-Aspect-Ratio, Thin/Flat/Cambered-Plate Wings," *Journal of Aircraft*, Vol. 37, No. 5, September 2000, pp. 825–832.

[8]Mueller, T. J. and Torres, G. E., "Low-Aspect-Ratio Wing Aerodynamics at Low Reynolds Numbers," *AIAA Journal*, Vol. 42, No. 5, May 2004, pp. 865–873.

[9]Torres, G. E. and Mueller, T. J., "Aerodynamic Characteristics of Low Aspect Ratio Wings at Low Reynolds Numbers," *Fixed and Flapping Wing Aerodynamics for Micro Air Vehicle Applications*, edited by T. J. Mueller, Vol. 195, Progress in Astronautics and Aeronautics, AIAA, Reston, VA, 2001, pp. 115–141.

[10]Spedding, G. R. and McArthur, J., "Span Efficiencies of Wings at Low Reynolds Numbers," *Journal of Aircraft*, Vol. 47, No. 1, January 2010, pp. 120–128.

[11]Frank, A., McGrew, J. S., Valentiz, M., Levinex, D., and How, J. P., "Hover, Transition, and Level Flight Control Design for a Single-Propeller Indoor Airplane," AIAA Paper 2007-6318, 2007.

[12]Sobolic, F. M. and How, J. P., "Nonlinear Agile Control Test Bed for a Fixed-Wing Aircraft in a Constrained Environment," AIAA Paper 2009-1927, 2009.

[13]How, J. P., "Multi-Vehicle Flight Experiments: Recent Results and Future Directions," *Proceedings of the Symposium on Platform Innovations and System Integration for Unmanned Air, Land and Sea Vehicles*, Neuilly-sur-Seine, France, 2007.

[14]Cory, R. and Tedrake, R., "Experiments in Fixed-Wing UAV Perching," AIAA Paper 2008-7256, 2008.

[15]Rhinehart, M. and Mettler, B., "Extracting Aerodynamic Coefficients using Direct Trajectory Sampling," AIAA Paper 2008-6899, 2008.

[16]Mettler, B., "Extracting Micro Air Vehicles Aerodynamic Forces and Coefficients in Free Flight Using Visual Motion Tracking Techniques," *Experiments in Fluids*, Vol. 49, No. 3, February 2010, pp. 557–569.

[17]Uhlig, D. V., Sareen, A., Sukumar, P. P., Rao, A. H., and Selig, M. S., "Determining Aerodynamic Characteristics of a Micro Air Vehicle Using Motion Tracking," AIAA Paper 2010-8416, 2010.


Copyright © 2012 by the author. Published by the American Institute of Aeronautics and Astronautics, Inc., with permission.

[18]Uhlig, D. V. and Selig, M. S., "Stability Characteristics of Micro Air Vehicles from Experimental Measurements," AIAA Paper 2011-3659, 2011.

[19]Serokhvostov, S. V. and Churkina, T. E., "One Useful Propeller Mathematical Model for MAV," *Proceedings of the International Micro Air Vehicles Conference and Flight Competition Summer edition*, Thales, Netherlands, 2011.

[20]Brandt, J. B., *Small-Scale Propeller Performance at Low Speeds*, Master's thesis, Department of Aerospace Engineering, University of Illinois at Urbana-Champaign, Urbana, IL, 2005.

[21]Veldhuis, L. L. M., "Review of Propeller-Wing Aerodynamic Interference," *24th International Congress of the Aeronautical Sciences*, Yokohama, Japan, 2004.

[22]Fratello, G., Favier, D., and Maresca, C., "Experimental and Numerical Study of the Propeller/Fixed Wing Interaction," *Journal of Aircraft*, Vol. 28, No. 6, June 1991, pp. 365–373.

[23]Catalano, F. M., "On the Effect of an Isolated Propeller Slipstream on Wing Aerodynamic Characteristics," *Acta Polytechnica*, Vol. 44, No. 3, March 2004, pp. 8–14.

[24]Witkowski, D. P., Johnston, R. T., and Sullivan, J. P., "Propeller/Wing Interaction," AIAA Paper 1989-0535, 1989.

[25]E-Flite, "Extra 260 3D Profile," `http://www.e-fliterc.com/Products/Default.aspx?ProdID=EFL2300`, Accessed November 2011.

[26]E-Flite, "UMX Extra 300 3D BNF," `http://www.e-fliterc.com/Products/Default.aspx?ProdID=EFLU1080`, Accessed November 2011.

[27]Rao, A. H., *Measurement of Aerodynamic Characteristics of MAVs Using Motion Tracking*, Master's thesis, Department of Aerospace Engineering, University of Illinois at Urbana-Champaign, Urbana, IL, 2012.

[28]Savitzky, A. and Golay, M. J., "Smoothing and Differentiation of Data by Simplified Least Squares Procedures," *Analytical Chemistry*, Vol. 36, No. 8, 1964, pp. 1627–1639.

[29]Stevens, B. L. and Lewis, F. L., *Aircraft Control and Simulation*, Wiley-Interscience, New York, NY, 2nd ed., 2006.

[30]Klein, V. and Morelli, E. A., *Aircraft System Identification: Theory and Practice*, AIAA Education Series, AIAA, Reston, VA, 2006.

[31]Tait, P. G., *An Elementary Treatise on Quaternions*, Cambridge at the University Press, Cambridge, United Kingdom, 3rd ed., 1890.

[32]McCormick, B. W., *Aerodynamics, Aeronautics, and Flight Mechanics*, John Wiley & Sons, New York, 2nd ed., 1995.

[33]Hepperle, M., *PropellerScanner Manual*, MH AeroTools, `www.mh-aerotools.de`, 2003.

[34]Roskam, J., *Airplane Flight Dynamics and Automatic Flight Controls*, Part I, DARcorporation, Lawrence, KS, 1995.


Copyright © 2012 by the author. Published by the American Institute of Aeronautics and Astronautics, Inc., with permission.